Applied Thermal Engineering 230 (2023) 120678

Contents lists available at ScienceDirect

Applied Thermal Engineering

journal homepage: www.elsevier.com/locate/apthermeng

Research Paper

Experimental investigation of the performance attributes of a thermal energy storage unit using different system configurations

Mohamed R. Salem *, Mohamed N. Owyed, Ragab K. Ali

Mechanical Engineering Department, Faculty of Engineering at Shoubra, Benha University, 108 Shoubra St., 11629 Cairo, Egypt

ARTICLE INFO

Keywords:
Thermal energy storage
Heat exchanger configuration
Effectiveness
Heat transfer augmentation

ABSTRACT

One of the goals engineers pursue in the energy production and recovery field is to design a heat exchanger that can store a large amount of thermal energy in a shorter time. This work practically tests the performance attributes of a latent heat thermal energy storage system in a vertical shell-tube heat exchanger configuration. Water flows in the tubes that are arranged as circular layers at certain radii in the shell, which is occupied by organic paraffin phase change material (RT60). The experiments consider the effects of the tube area ratio, layer radius ratio, number of tube layers, and distribution of the tubes (inline/staggered), besides incorporating semicircular tubes instead of complete circular ones. These experiments are conducted by employing heating water (65 °C to 75 °C) during the charging process and cooling water (25 °C) during the discharging process. The key findings from this work are that increasing the radius ratio from 1/3 to 2/3, employing semicircular tubes instead of complete ones, increasing the area ratio from 2.4% to 4.3%, and distributing the same number of tubes in two layers rather than one layer provide reductions in the charging time of 7.2%, 7.3%, 17.6%, and 11%, respectively. The corresponding augmentations in the charging/discharging effectiveness are 8.1%/2.6%, 7.4%/3.3%, 19.7%/5.7%, and 8%/4.5%, respectively. Moreover, by applying a staggered distribution of the tubes instead of an inline one, the charging effectiveness is amplified by 5.3%. Finally, a set of experimental correlations is developed to predict the charging effectiveness of the storage system.

1. Introduction

Thermal energy storage (TES) is one of the crucial technologies to address global energy challenges by improving energy efficiency and achieving energy savings. These systems can be incorporated to conserve the heat from solar energy sources such as concentrated solar power plants and to store the waste heat from industrial processes such as oil, cement, ceramic, steel, and glass industries, which are considered major waste heat sources [1]. Therefore, TES systems offer promising solutions to the world's energy problem, as this technology plays an important role in the deployment of energy utilization, especially for renewable energy. The usage of TES systems often achieves significant benefits, such as reducing energy consumption and costs, more effective utilization of equipment, and facilitating more efficient energy use, in addition to reducing pollutant emissions [2].

The heat energy can be stored and then used later by using sensible heat storage systems in which there is a noticeable change in the temperature of the storage medium, such as concrete or water. On the other hand, employing phase change material (PCM) as a latent heat thermal energy storage (LHTES) system can provide a higher energy density, less system mass, and a more stable operating temperature compared with sensible heat storage systems. Paraffin compounds are a common PCM used in LHTES systems. It has comparatively considerable latent heat, is safe and noncorrosive, and its stability of thermophysical properties does not change significantly after many cycles of melting and solidification. But its low thermal conductivity (0.1–0.4 W/m.°C) can be a drawback in high-power applications [2]. Thus, the performance of LHTES systems during the charging/discharging processes is strongly influenced by the PCM's poor thermal conductivity. Therefore, some advanced heat transfer enhancement techniques need to be developed to overcome this common shortcoming for TES applications. To obtain more effective TES systems, various techniques have been suggested, which are classified as active/passive techniques [1–3].

Numerous investigations [3–8] considered the addition of solid nanoparticles to the PCM. Compared with a pure medium, the thermal conductivity, and viscosity of the proposed mixture were increased; however, the phase change enthalpy, melting point, and specific heat were dropped. Besides, numerous studies have considered the effect of geometrical and operational parameters on LHTES systems. Mosaffa

* Corresponding author.
E-mail addresses: me_mohamedreda@yahoo.com, mohamed.abdelhamid@feng.bu.edu.eg (M.R. Salem).

https://doi.org/10.1016/j.applthermaleng.2023.120678
Received 14 January 2023; Received in revised form 3 March 2023; Accepted 28 April 2023
Available online 4 May 2023

Nomenclatures

A	Area,m^2
C	Specific heat,J/kg.°C
D	Diameter, m
L	Length, m
$\dot{m}$	Mass flow rate,kg/s
m	Mass, kg
N	Number of tube layers
n	Number of tubes
Q	Heat transfer rate, W
T	Temperature, °C or K
t	Time, s
V	Volume,m^3
$\dot{V}$	Volume flow rate,m^3/s

Dimensionless groups

Fo	Fourier number
St	Stanton number

Greek letters

λ	Radius ratio
Δ	Differential
ω	Uncertainty
α	Thermal diffusivity,m^2/s
ε	Effectiveness
θ	Tubes distribution angle, °
π	Pi ≡ A mathematical constant ≅ 3.1416
ρ	Density,kg/m^3
ϕ	Area ratio

Superscripts and subscripts

abs	Absorbed
ch	Charging
disch	Discharging
e	External
i	Element Number
in	Internal
initial	Initial value
L	Liquid phase
l	Latent
m	melted
max	Maximum
ph	Phase change
s	Solidified/Solid phase
sens	Sensible
sh	Shell
st	Stored
T	Total
t	Tube

Acronyms and abbreviations

AR	Arrangement
HTF	Heat Transfer Fluid
HTFT	Heat Transfer Fluid Temperature
LH	Latent Heat of the PCM,J/kg
LHTES	Latent Heat Thermal Energy Storage
MMF	Melted Mass Fraction
PCM	Phase Change Material
SMF	Solidified Mass Fraction
TES	Thermal Energy Storage

et al. [9] analytically studied the PCM solidification in a finned shell-tube TES system using cylindrical and rectangular shell geometries. The findings referred to the fact that cylindrical orientation was more effective during PCM solidification. In addition, the inlet temperature of the heat transfer fluid (HTF) was more dominant than its velocity. The latter result was also confirmed by Korti and Tlemsani [10]. Tay et al. [11] optimized a tube-in-tank LHTES system using a validated effectiveness-NTU model. The results showed that the system stored useful energy at a rate 18 times greater than that of sensible storage systems per unit volume. Hosseini et al. [12] considered the performance improvements that resulted due to natural convection during the PCM melting phase in a heat exchanger of the shell-tube type. Guelpa et al. [13] simulated and analyzed a shell-and-tube LHTES system for both un-finned/finned configurations. The finned model reduced the solidification time of the PCM and boosted the second-law efficiency. Avci and Yazici [14] investigated the PCM/water shell-tube LHTES system performance. According to the authors, increasing/decreasing the heat transfer fluid temperature (HTFT) within the melting/solidification processes augmented the phase change process. Mahfuz et al. [15] showed that increasing the HTF flow rate improved the LHTES system efficiency. Kamkari et al. [16] investigated PCM melting in an enclosure of rectangular configuration at various inclination angles. As indicated, the natural convection currents and the overall PCM melting time were significantly affected by the angle of inclination. Besides, the horizontal enclosure's heat transfer enhancement ratio was two times higher than that of the vertical one.

Hosseini et al. [17] demonstrated the characteristics of heat transfer during paraffin RT50 melting/solidification in a shell-tube heat exchanger. The obtained results indicated that increasing the HTFT from 70 °C to 80 °C augmented the charging/discharging efficiencies by 9% and 2.1%, respectively. Sun et al. [18] analyzed the performance of LHTES. The authors attributed the change in behavior to the change in the natural currents. Abujas et al. [19] numerically simulated the performance of the LHTES system (finned pipes and conductive foams). It was found that conductive foams showed better performance and a shorter charging time than fins. Seddegh et al. [20] constructed a shell-tube heat exchanger as an LHTES and performed tests for both horizontal and vertical orientations. The results showed that increasing the HTFT shortened the melting time, while its flow rate had a tiny effect. Moreover, horizontal orientation showed higher overall performance. Han et al. [21] modelled the melting process of PCM in shell-tube LHTES systems. The author stated that the upward flow of the HTF in the vertical orientation resulted in a higher heat storage rate than that in the downward direction. Tayssir et al. [22] tested the melting behavior of paraffin wax in a vertical shell and helical coil TES system. The authors also assured that the HTF flow rate is the dominant parameter rather than its temperature. Mahdi et al. [23] investigated the paraffin wax behavior during the melting process within a shell-tube LHTES system with various configurations. The authors referred to the natural convection currents as playing an important role during PCM melting. Also, the horizontal orientation was more efficient than the vertical one. Deng et al. [24] examined the performance of a finned-LHTES system. The results indicated that longer fins greatly improved the system's performance. In addition, the melting time was reduced by 50% by increasing the HTFT by 20 °C. Mehta et al. [25] experimentally tested the vertical and horizontal orientations of an LHTES system. The results also assured that the horizontal model was better than the vertical one as it needed less time to melt half of the PCM. Furthermore, the HTFT had a great influence during both PCM melting/solidification.

Fornarelli et al. [26] theoretically presented a model to predict melting time in an LHTES system using a shell-tube heat exchanger type. It was revealed that increasing the radial ratio (the external radius over the internal radius) reduced the overall melting time. Mahdi et al. [27] numerically compared the effects of the insertion of fins and/or

aluminium oxide nanoparticles in a PCM medium. The results demonstrated that combining nanoparticles with PCM was an inefficient procedure. Pakalka et al. [28] compared and assessed experimentally the working of two PCM-finned tube heat exchangers with distinct geometrical parameters. The investigation showed that both configurations nearly achieved similar results, regardless of the production complexity and cost. Zhang et al. [29] studied numerically the PCM melting process in the finned LHTES unit. It was shown that the fin structure and the HTF velocity had a substantial impact on the melting process. Furthermore, it was better for the LHTES system if the HTF direction was opposite to the acceleration of gravity. Bazai et al [30] numerically investigated an annulus with an inner ellipse as a TES system. The outer wall is insulated while the inner one is isothermal. The results showed that the lowest aspect ratio has the best performance during charging phase, while the aspect ratio does not have a significant impact on the solidification process. Elsanusi and Nsofor [31] conducted numerical simulations to investigate the performance attributes of multiple PCMs for different arrangements in a horizontal heat exchanger during melting of the PCMs. It was found that the application of multiple PCMs has better effects on the heat transfer mechanisms and the heat storage capacity. Furthermore, natural convection has a significant positive effect on the heat transfer characteristics of these systems and shortened the total melting time. He et al. [32] experimentally incorporated foam fin in the PCM to overcome the poor thermal conductance of PCM in vertical shell-tube LHTES unit. Three shapes of the fins were tested at three different HTF flow rates. Experimental outputs showed significant increases in the thermal performance as the melting rate was augmented by 14.1%, while the flow rate of the HTF had a small influence on the temperature response rate.

Peng et al. [33] established a numerical model to simulate the consequence of integration of fractal tree-like fins into an LHTES unit. The results revealed that the fins significantly accelerated the melting process, which reduced its time by 64.3%. Rodrigues and de Lemos [34] experimentally investigated the discharge effectiveness of an LHTES system. A packed bed of rocks served as the storage medium. Results indicated that increasing the cooling airflow, increasing the porosity, and decreasing the permeability improved the associated effectiveness. Li et al. [35] experimentally and numerically compared the effect of incorporating fins or foam in the PCM on the effectiveness of a vertical double pipe LHTES system. This research showed that the introduction of a special fin, characterized by thermal conductivity via a microfluidic layer, can offer an excellent increase in power density during charging, while being easier to process and cheaper to manufacture for industrial applications compared to metal foams in a complex microstructure. Shen et al. [36] practically investigated the charging attributes of low-temperature finned cascaded (shell-three-tube) LHTES unit. It was shown that the rate of temperature growth and energy loaded of the 1st stage were considerably higher than those of the later stages. Huang et al. [37] completed simulations and practical tests on a low-temperature LHTES unit for solar thermal storage. Ali [38] synthesized hybrid PCMs and tested them as a solar TES unit. The author considered in his research the major problems associated with PCMs, such as cost, corrosion/erosion, and instability. Mao and Zhang [39] simulated the thermal performance of a cascade vertical LHTES tank. The proposed cascade system resulted in improving the storage energy by about 42%. Zou et al. [40] experimentally compared the thermal performance of the sensible/latent thermal energy storage units, with/without the integration of foam fin in the PCM. The obtained results showed a higher performance for the latent storage rather than the sensible one. Besides, conducting the cooper foam resulted in an extra higher thermal efficiency. Lv et al. [41] practically tested the LHTES system on a pilot scale with/without fins of different shapes in the PCM. The authors took into account the outlet temperature of the HTF during the charging phase. It was shown that the temperature difference in the vertical orientation of the LHTES system was larger than in the horizontal one.

As a result of changing the required thermal loads in numerous applications, there may be a large deficit at certain times, while at other times the thermal energy may be abundant and overflowing. Therefore, there is still an urgent need to augment the effectiveness of TES and recovery systems. In general, most previous research confirms that the performance characteristics of the horizontal heat exchanger are slightly better than those of the vertical heat exchanger during TES processes. However, since the vertical heat exchanger is easier to operate, maintain, disassemble, and install, the vertical orientation allows for consistent visibility, ease, and greater accuracy in the methods of calculations and analysis. This is also due to the presence of many identical elements, which facilitate measurements and calculations. Therefore, emphasis is placed here on using a vertical heat exchanger (to some extent), as it requires more improvement in its performance as well as ensuring the accuracy of the results.

Moreover, from the above survey, it is clear that most of the previous research focused on using the shell-tube heat exchanger as a TES system but neglected to study the distribution effect of the inner tubes used for heat transfer from/to the hot/cold water during the PCM melting/solidification process, although their distribution may be a key solution to overcome the poor thermal conductance of the PCM. This proposed enhancement method is a promising passive, more applicable and cheap technique. Therefore, this work practically tests the performance attributes of an LHTES system with a vertical shell-tube heat exchanger configuration. The internal tubes are straight and arranged as circular layers at certain radii in the shell, which is occupied by PCM, while water flows in the tubes in an upward direction. The experiments consider the effects of the number of tubes (area ratio ϕ), the position of the tube layer (radius ratio λ), the number of tube layers (N), and the distribution of the tubes in the shell (inline/staggered). Besides, the effect of incorporating SCTs instead of CCTs is examined. These experiments are conducted during the charging/discharging process at different HTFTs, which correspond to a wide range for the PCM Stefan Number (St).

2. Experimental apparatus

The apparatus used in this investigation consists of a heating unit, a cooling unit, a shell-straight tube heat exchanger (the PCM is on the shell side while the HTF flows through the tubes), a pump, valves, a flow meter, T-type thermocouples, digital thermostats, and pipes connecting all these parts. Fig. 1 provides the layout of the whole setup, while Fig. 2 introduces a photo of the present setup. Each of the heating and cooling units has a well-thermally insulated 20-liter stainless steel tank. An electric heater with a maximum rating of 6 kW is fixed in the heating tank to heat the water to the required temperature, while the heat is removed from the cooling tank water by a cooling device of 5.2 kW capacity. The operations of the two units are regulated by digital thermostats, which are used to keep constant temperatures in the HTF entering the heat exchanger. There are three ports in each tank: two of them are on the top cover of the tank, which represents the inlet ports from the heat exchanger and the bypass line. The other port is at the bottom of the tank and represents the exit port for the pump.

Seven configurations of the shell-straight tube heat exchanger were used in this study. The shell is a cylinder fabricated from 2 mm-thick galvanized steel with 120 mm and 150 mm internal diameter and length, respectively. The incorporated tubes are made of copper material with 9.52 mm and 8.3 mm external and internal diameters, respectively. The characteristic dimensions of the different configurations are illustrated in Table 1 and indicated in a schematic diagram in Fig. 3, while Fig. 4 shows schematic diagrams for the seven shell-tube heat exchangers. Two dimensionless parameters are established in the existing work: the area ratio (ϕ), which expresses the ratio between the cross-section area of the internal tubes ($n A_t$) to that of the shell (A_{sh}), and the radius ratio (λ), which expresses the ratio between the layer diameter (D_{Layer}) to that of the shell ($D_{sh,in}$), defined as follows:

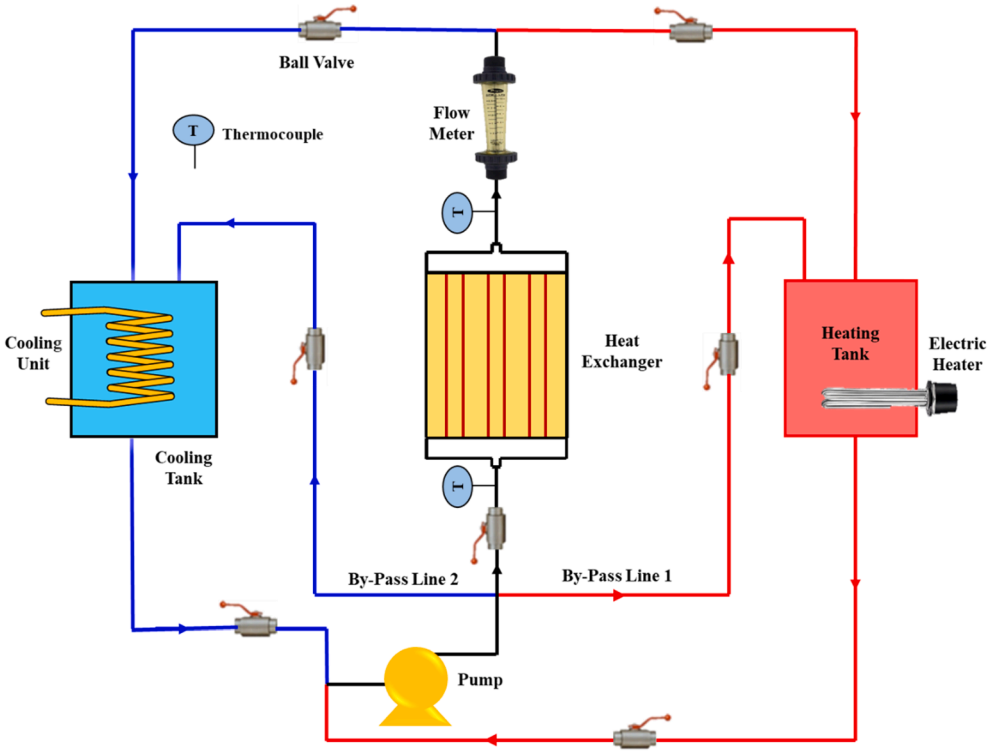

Fig. 1. A layout of the whole setup.

1 Test section
2 Upper cabinet
3 Lower cabinet
4 Heating tank
5 Electric heater
6 Cooling tank
7 Digital thermostat
8 Thermocouples
9 Flowmeter
10 Pump
11 Connecting pipes
12 Ball valves

Fig. 2. A photo of the present experimental apparatus.

$$\phi = \frac{nA_{t,o}}{A_{sh,in}} = \frac{nD_{t,o}^2}{D_{sh,in}^2} \quad (1) \qquad \lambda = \frac{D_{Layer}}{D_{sh,in}} \quad (2)$$

Table 1
Characteristic dimensions of the different configurations.

AR	Shape	$D_{sh,in}$ (mm)	L (mm)	$D_{t,o}$ (mm)	$D_{t,in}$ (mm)	N	θ	n	ϕ	λ
#1	CCT	120	150	9.52	8.3	1	90°	5	0.024	1/3
#2										1/2
#3										2/3
#4							45°	9	0.043	2/3
#5						2	90°			1st layer. λ = 1/3
#6							45°			2nd layer. λ = 2/3
#7	SCT					1	90°	5	0.024	2/3

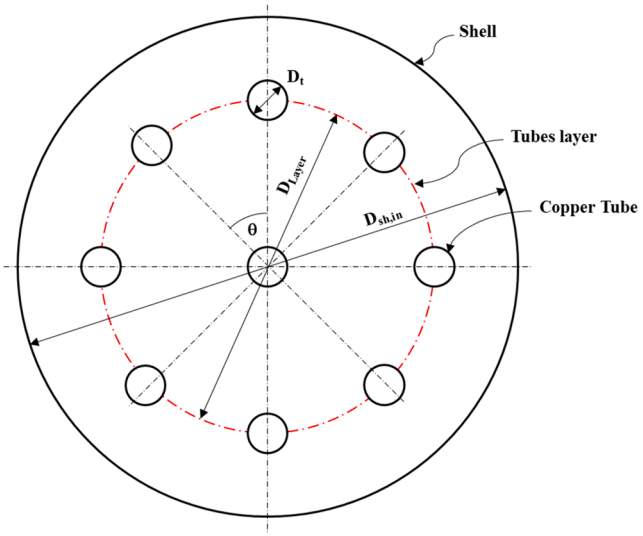

Fig. 3. Characteristic dimensions of tested configurations.

Two cabinets are employed in the existing test rig, manufactured from galvanized steel (2 mm wall thickness), to collect the water to/from the tubes. The cabinets have a diameter and length of 120 mm. Two flanges of 220 mm diameter and 4 mm wall thickness of the same material are bolted to the flanges of the PCM shell. Wholly, 14 housing dies are fabricated from acrylic circular sheets of 180 mm diameter and 6 mm wall thickness and are located between the cabinet and PCM in the shell. A laser cutting machine is utilized to drill the housing dies, forming holes of the same dimensions and number of tubes as the tubes in the incorporated tube bundle. A sample of the housing dies is presented in Fig. 5. Also, the entering and departure ports of the two cabinets are tubes of 100- and 12-mm length and internal diameter, respectively, which are soldered to the two cabinets. Furthermore, two rubber gaskets are incorporated into each cabinet to prevent any leakage; they are placed on the two surfaces of the housing die. Attention is considered to be paid to sealing off any gap between the tubes and the holes in the housing dies.

An organic paraffin PCM type (RT60: Rubitherm GmbH (CnH2n + 14)) is utilized in the current investigation with technical specifications, as illustrated in Table 2. These specifications are introduced by the manufacturer data sheet and Tayssir et al. [22]. Firstly, the PCM is liquefied through a heating process in a water basin, as described by Salem et al. [3], until it reaches its melting point. Noting that the melting point of the PCM is checked experimentally in the laboratory by inspecting the time interval of the mushy zone during the PCM liquefaction/solidification processes, the temperature of the PCM is recorded with time during the upscale sequential test (liquefaction process) besides the downscale sequential test (solidification process), and the results are demonstrated in Fig. 6. It is recorded that the limits of the mushy zone correspond to temperatures of 55.6 °C and 61.3 °C in the upscale sequential test, while the corresponding values in the downscale sequential test are 60.7 °C and 54.9 °C. The average temperature over this period in both tests is determined at 58 °C, which is taken as the PCM melting point during this study.

Polyvinyl chloride pipes and flexible nylon connections are used to connect all parts of the test rig, except the copper tubes in which the HTF flows through the heat exchanger. A 0.5-hp power rating centrifugal pump is engaged to circulate the hot water in the heating loop between the heating tank and the heat exchanger during the charging process, and to pump the cold water into the cooling loop between the cooling tank and the heat exchanger during the discharging process. A calibrated variable area flow meter (1.8–18 l/min flow rate range and an accuracy of ± 5% of the reading) is employed to measure the volume flow rate of the HTF. The calibration process for the flow meter was done in the laboratory by running water at a rate of 15 l/min. The calibration process was repeated three times, and the results showed tiny differences between them. Their average value, 15.28 l/min, is taken as the best estimate of the rotameter in this reading. T-type thermocouples (wires of 0.2 mm diameter) are used to measure the temperatures at the energy storage unit. Four thermocouples are directly inserted into the HTF flow stream at the heating and cooling tank ports to measure the inlet and exit temperatures in each tank. The other thermocouples (between six and eleven according to the tested heat exchanger arrangement as presented in Fig. 4) are inserted at different positions in the PCM to measure their temperatures over the testing time. The thermocouples are connected to a data acquisition system to record the temperatures on the laptop. The entire system for temperature measurement is calibrated for each thermometer, which can be correctly read to ± 0.5 °C.

3. Experimental procedures

In this investigation, seven arrangements of the tested heat exchanger were considered, and three experiments were conducted for each, covering three charging inlet temperatures of the HTF, which correspond to three different PCM Stefan numbers as demonstrated in Table 3. Furthermore, each experimental run comprises two processes: charging (PCM melting) and discharging (PCM solidification). Initially, the heating and cooling cabinets are filled with water, while the shell is filled with liquefied PCM. Then the system parts are gathered: the heat exchanger, cooling/heating cabinets, pump, connecting piping, flow meter, valves, and thermocouples. Next, the chilling unit and pump are operated to pass the cooling water (25 °C, 15.28 l/min) through the cooling loop. This step is stopped after the temperatures at different locations in the PCM read nearly 25 °C. Now that the whole PCM is in the solid phase, the charging process can be considered. In the charging process, the first step is to turn on the electric water heater, which is adjusted by setting its thermostat. While the water flow rate is manually evaluated using the flowmeter and the accompanying valves.

The PCM in the shell is divided into small elements, which are surrounded by a group of thermocouples. Once the average temperature of any element reaches its melting point (58 °C), this is considered the time for the onset of melting. Now, the charging process is being considered to begin, in which the temperatures at different locations in the system are recorded along with time. The recording of the system temperatures is continued until no change in the HTF outlet temperature occurs for 20

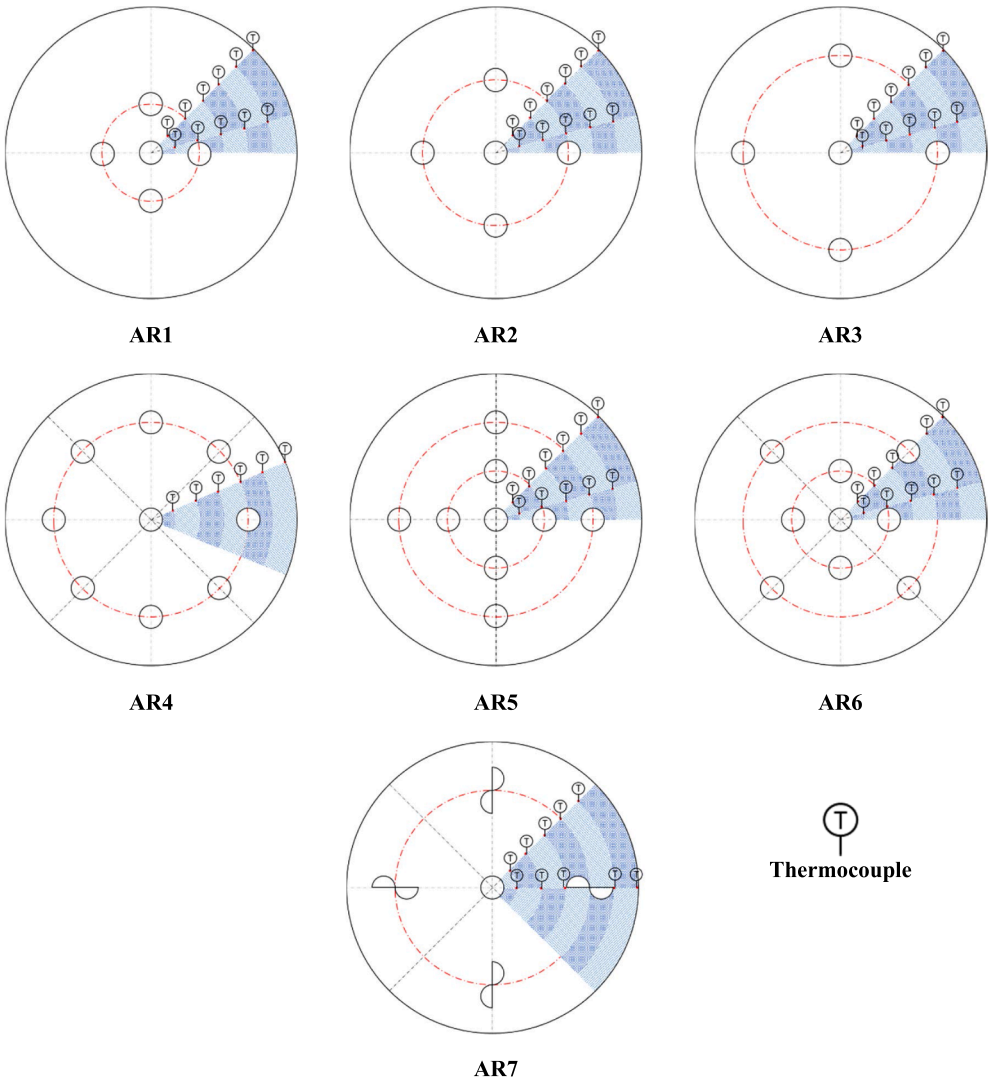

Fig. 4. Schematic diagrams of the tested LHTES configurations.

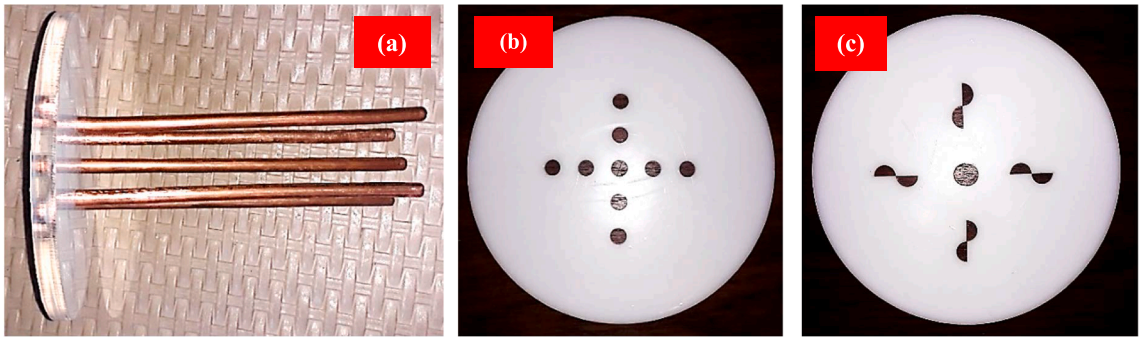

Fig. 5. Photos of a sample of (a) the tubes and housing die (b) AR5 and (c) AR7.

min and/or until the lowest local temperature of the PCM reaches its melting point (58 °C) to ensure nearly the overall melting of the entire PCM quantity. At this step, the charging process is considered to be finished, the total time for the charging process is documented, and then the heating loop is turned off. To simultaneously start the discharge process, the cooling unit is turned on during the charging process. This is to maintain a constant temperature of the water in the cooling tank at 25 °C with the aid of the cooler thermostat. After finishing the charging process, the heating loop is shut down and the cooling loop is simultaneously opened by adjusting the specified cooling water volume flow at a rate of 15.28 l/min. Now, the discharging process is considered to have begun, in which the temperatures at different locations in the system are recorded along with time. The system temperatures are continued to be documented until no change in the HTF outlet temperature occurs for 20 min and/or until the highest local temperature of the PCM reaches its solidifying point (58 °C) to ensure nearly the overall solidification of the entire PCM quantity. At this step, the discharge process is considered to be finished, the total time for this process is

Table 2
Characteristic specifications of the utilized PCM [22].

Type	RT60
Melting point (°C)	55–61
Heat of fusion (kJ/kg)	168
Thermal conductivity (W/m·°C)	0.2
Density (kg/m^3)	Solid. 930 Liquid. 830
Specific heat capacity (kJ/kg·°C)	Solid. 2.1 Liquid. 2.5
Kinematic viscosity (mm^2/s)	34.9
Volume expansion (%)	12.5

documented, and then the heating loop is turned off. A Microsoft Excel sheet is prepared to process the melted and solidified masses, mass fractions besides the stored/absorbed heat energy, and the effectiveness at different times during the charging and discharging processes, respectively.

4. Calculation methodology

In this work, the total PCM volume is radially divided into small elements. Each of them is surrounded by several thermocouples, as indicated in Fig. 4. The average value of their local readings is considered the element temperature. After recording the readings of thermocouples for each experiment, the following relationships are utilized to assess the performance of the conducted arrangement. The total PCM mass (m_T) is calculated from Eq. (3) as a function of the PCM density in the solid phase (ρ_s) and its volume.

$$m_T = \rho_s \left[\frac{\pi}{4}\left(D_{sh,in}^2 - nD_{t,o}^2\right)\right] L_{PCM} \tag{3}$$

During the charging process, the variation of the melted mass of PCM with time is estimated by summing the mass of melted elements (whose average temperature is higher than the melting point) at each time. Now, the melted mass fraction (*MMF*) can be calculated as a ratio of the melted mass (m_m) and the total mass of PCM. In Eq. (4), $m_{m.i}$ and $V_{m.i}$ are the mass and volume of the melted PCM element, respectively.

$$m_m = \sum m_{m.i} = \rho_s{}^* \sum V_{m.i} \tag{4}$$

$$MMF = \frac{m_m}{m_T} \tag{5}$$

Additionally, the amount of stored thermal energy (Q_{st}) after any period can be estimated as a summation of the energy stored within each element ($Q_{st.i}$) as indicated in Eq. (6). It should be noted that if the average temperature of an element is less than or equal to its melting point, the stored heat can be calculated as sensible heat as provided in Eq. (7). However, if the average temperature of an element is higher than its melting point, the heat stored can be estimated by summing the sensible and latent heats, as illustrated in Eq. (8).

$$Q_{st} = \sum Q_{st.i} \tag{6}$$

$$Q_{st.i} = m_i C_s (T_i - T_{initial}) \text{For} T_i \le T_{ph} \tag{7}$$

$$Q_{st.i} = m_i C_s \left(T_{ph} - T_{initial}\right) + m_i LH + m_i C_L \left(T_i - T_{ph}\right) \text{For} T_i \ge T_{ph} \tag{8}$$

Besides, the maximum possible energy (Q_{max}) that can be stored within the PCM is calculated as the sum of all sensible and latent heats, Eq. (9). While the charging effectiveness (ε_{ch}) is estimated as the ratio between the actual total and the maximum heat energy stored within the PCM, Eq. (10), where T_{HTF} is the inlet temperature of the heat transfer fluid (water).

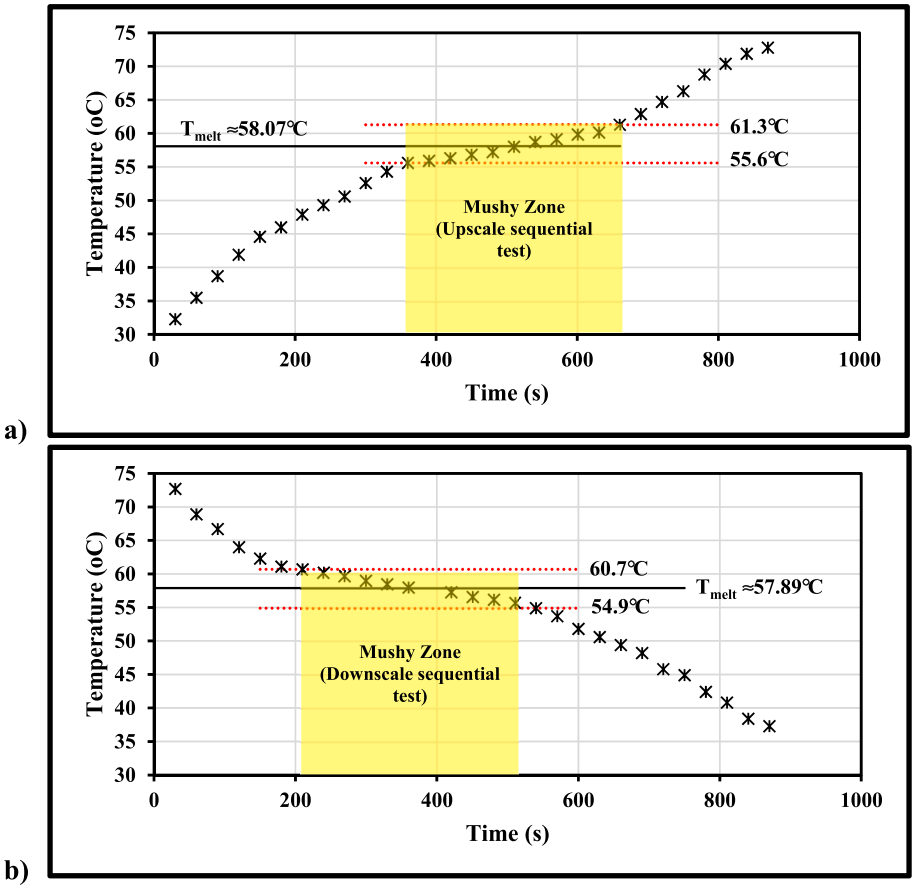

Fig. 6. PCM melting point determination test.

Table 3
Experiments working conditions.

No.	Arrangement	Charging process		Discharging process		HTF Flow Rate (l/min)
		HTFT (°C)	PCM Stefan Number (St)	HTFT (°C)	PCM Stefan Number (St)	
1	1	65	0.096	25	0.452	15.28
2		70	0.164			
3		75	0.233			
4	2	65	0.096			
5		70	0.164			
6		75	0.233			
7	3	65	0.096			
8		70	0.164			
9		75	0.233			
10	4	65	0.096			
11		70	0.164			
12		75	0.233			
13	5	65	0.096			
14		70	0.164			
15		75	0.233			
16	6	65	0.096			
17		70	0.164			
18		75	0.233			
19	7	65	0.096			
20		70	0.164			
21		75	0.233			

$$Q_{max} = m_t C_s\left(T_{ph} - T_{initial}\right) + m_t LH + m_t C_L\left(T_{HTF} - T_{ph}\right) \tag{9}$$

$$\varepsilon_{ch} = \frac{Q_{st}}{Q_{max}} \tag{10}$$

For the discharging process, the solidified mass (m_s) is the sum of the masses of elements whose average temperature is less than the phase change temperature. The solidified mass fraction (*SMF*) can be calculated as the ratio between the solidified and total mass of PCM as follows:

$$m_s = \sum m_{s.i} = \rho_s \sum V_{s.i} \tag{11}$$

$$SMF = \frac{m_s}{m_T} \tag{12}$$

In addition, the thermal energy absorbed (Q_{abs}) after any period can be estimated as the sum of the energy absorbed from each element ($Q_{abs.i}$) according to Eq. (13). Noting that if the average temperature of an element is higher than the phase change temperature, the heat absorbed can be calculated as a sensible heat as shown in Eq. (14), while if its average temperature is less than or equal to the phase change temperature, the heat absorbed can be estimated as the sum of the sensible and latent heats as demonstrated in Eq. (15), in which T_{intial} is the initial average temperature of the element.

$$Q_{abs} = \sum Q_{abs.i} \tag{13}$$

$$Q_{abs.i} = m_i C_L (T_{initial} - T_i) \text{For} T_i \geq T_{ph} \tag{14}$$

$$Q_{abs.i} = m_i C_L (T_{initial} - T_i) + m_i LH + m_i C_s\left(T_{ph} - T_i\right) \text{For} T_i \leq T_{ph} \tag{15}$$

Moreover, the discharging effectiveness (ε_{disch}) is estimated as the ratio between the actual total and the maximum heat energy released by the PCM, Eq. (16). Furthermore, the dimensionless time (Fourier number) is determined using Eq. (17) [22] and considers the proportion of diffusive or conductive transport rates to the storage rate through the PCM in the shell. Besides, the PCM Stefan Number, which judges the ratio of sensible and latent heat, is determined using Eq. (18) [22], in which $C = C_L$ is for the charging process and $C = C_s$ is for the discharging process.

$$\varepsilon_{disch} = \frac{Q_{abs}}{Q_{max}} \tag{16}$$

$$Fo = \frac{\alpha t}{D^2_{sh,in}} \tag{17}$$

$$St = \frac{C\left(T_{HTF} - T_{ph}\right)}{LH} \tag{18}$$

5. Uncertainty analysis

The primary parameters used to interpret the experimental results in this study are functions of many variables, including laboratory measurement data and physical properties. The error associated with each of these measured quantities is accounted for to quantify the uncertainty properly. The accuracy of a sensor contributes to the uncertainty of a measurement conducted by this sensor, and this accuracy can be obtained through either the manufacturer's specifications or calibration procedures. According to the manufacturer, there is a ± 0.1 mm margin of error in the diameters of the internal tubes, while the uncertainty in the other measured diameters and lengths is considered to be ± 0.5 mm. Furthermore, the charging/discharging time estimation has a ± 1 s error margin. Furthermore, the uncertainty in the thermophysical properties of the cooling/heating water and PCM is taken as ± 0.1%. For all experimental runs, the uncertainties in the main parameters are determined using Kline and McClintock [42] methodology and summarized in Table 4. For the estimated uncertainties in the other variables and parameters used in the present study, additional information is given in Appendix A.

6. Apparatus validation and data verification

Concerning the aforesaid experimental and analysis methodologies, the verification of the procedures in determining the charging effectiveness of the LHTES system is implemented, and the resulting values are compared with those of the system developed by Seddegh et al. [20] with a concentric tube heat exchanger (n = 1). The specifications of the validation process are revealed in Table 5, while the results of this comparison are shown in Fig. 7. It is clear that the experimental results for charging effectiveness deviate by an average value of ± 13.2% from those of Seddegh et al. [20]. This good agreement in comparison reveals the accuracy of the experimental set-up and measurement techniques.

7. Results and discussions

A series of experiments are carried out, in which HTF (water) is passed through the tubes while paraffin wax is in the shell surrounding the tubes. In total, 21 experiments were done for both the charging and the discharging processes on the seven heat exchanger arrangements. The thermal performance results are presented for the different governing parameters such as molten/solidified mass, mass fraction, stored/absorbed heat energy, and charging/discharging effectiveness during the melting/solidification processes, respectively. The temperatures at different locations within the paraffin wax are recorded during each experiment. Fig. 8 provides a sample of the temperature allocation within the wax in AR1 at locations 1 and 10. The presented values are for

Table 4
Uncertainties in the main parameters.

Parameter	Maximum Uncertainty (%)
Mass (m)	±0.95
Melted mass fraction (*MMF*)	±1.34
Solidified mass fraction (*SMF*)	±1.34
Heat energy (Q)	±1.11
Charging/Discharging effectiveness (ε)	±1.57

Table 5
Specifications of the validation process.

Specifications		Seddegh et al. [20]	Present
PCM	Type	RT50	RT60
	Latent heat (kJ/kg)	168	168
	Average melting temperature (°C)	48	58
HTF	Type	Water	Water
	HTFT (°C)	75	75
	Reynolds number	964.2	964.2
Number of internal tubes, n		1	1
Heat exchanger orientation		Vertical	Vertical

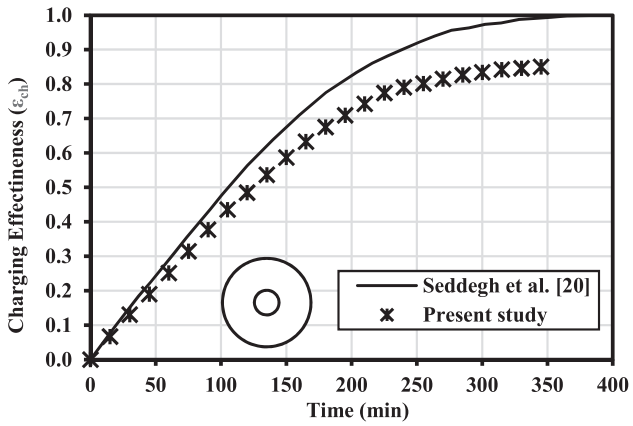

Fig. 7. Results of the validation process for charging effectiveness.

HTFT of 70 °C and 25 °C during the charging and discharging processes, respectively.

7.1. Effect of HTF charging temperature

In this analysis, three different HTFTs (65, 70, and 75 °C) are considered for the seven LHTES systems. These temperatures correspond to PCM Stefan numbers of 0.096, 0.164, and 0.233, respectively. Fig. 9 illustrates the melted mass fraction (*MMF*), accumulated stored heat, and charging effectiveness at different charging times for AR3 as a sample of the obtained results. It is seen that increasing the *HTF* charging temperature reduces both the total charging time and the time at which the melting begins, and it increases the melted mass, *MMF*, accumulated stored heat, and charging effectiveness. The average percentage variation due to increasing the inlet temperature of the HTF during the charging process is summarized in Table 6.

These results can be due to increasing the temperature difference between the *HTF* and the PCM by increasing the HTFT, which boosts the sensible heat that can be added to the PCM. Consequently, the heat exchange process is improved, the charging time is decreased, and the total stored heat as well as the charging effectiveness is augmented. Furthermore, it is obvious in Fig. 9a and 9b that the melted mass remains at zero value for a period at the beginning of the charging process. This occurs as the PCM temperature is below its melting point. After reaching the phase change temperature, the latent heat exchange begins, and the melted mass increases with time. Moreover, Fig. 9c and 9d show that the slopes of the accumulated stored heat and effectiveness curves are small at the beginning of the charging process while they grow subsequently. This occurs as the thermal energy stored in the PCM at the start of the charging process is a sensible heat until some PCM elements reach their phase change temperature. Afterward, the latent heat, which is larger than sensible heat, is considered in the accumulated stored energy and the charging effectiveness calculations. Also, the natural currents, which appear after some PCM melting, boost the stored heat and the system's thermal performance, as the heat transfer is altered from conduction mode only to conduction and convection modes simultaneously.

7.2. Effect of heat exchanger configuration on the charging process

The seven arrangements of the tested heat exchanger, mentioned in Table 1 and Fig. 4, are examined during the charging process at various HTFTs (65, 70, and 75 °C), which correspond to different PCM Stefan Numbers (0.096, 0.164, and 0.233). Fig. 10 records the obtained results for melted mass, *MMF*, and accumulated stored heat, besides the

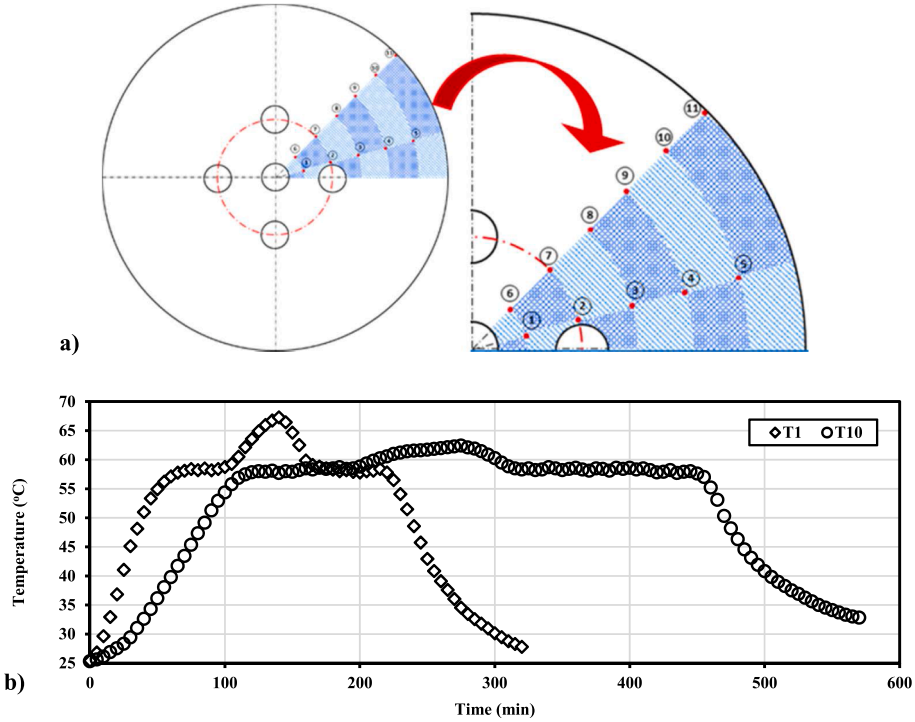

Fig. 8. AR1. a) Thermocouple locations; b) Temperature distribution.

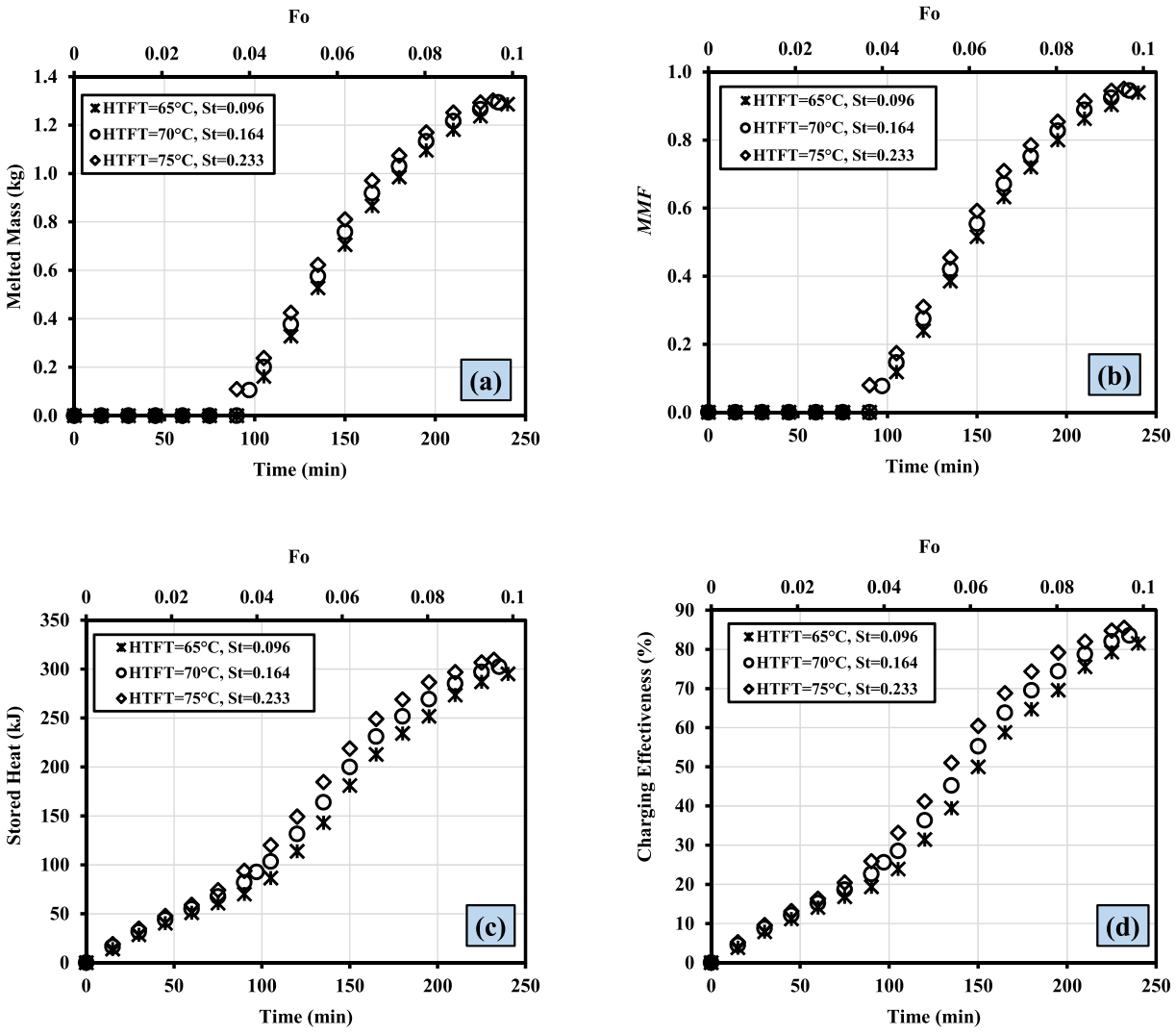

Fig. 9. Performance parameters of tested LHTES systems charging time; (a) Melted mass, (b) *MMF*, (c) Stored heat, and (d) Charging effectiveness.

Table 6
Effect of HTF charging temperatures.

Specifications	Increase of HTF charging temperature from 65 to 70 and 75 °C	
	Average percentage of variation	
	HTFT = 70 °C	HTFT = 75 °C
Total charging time	−2.2%	−4.3%
Melting beginning time	−3.9%	−7.8%
MMF	+0.7%	+1.4%
Charging effectiveness	+2.8%	+5.4%

charging effectiveness at different charging times for the inlet temperature of the water of 75 °C (St ≈ 0.233), as a sample of the obtained results. It is revealed that the system performance is improved by increasing the tube radius ratio (λ) from 1/3 to 2/3, incorporating SCTs instead of circular ones, increasing the number of internal tubes (area ratio ϕ) in the heat exchanger, and applying a staggered distribution ($\theta = 45^{\circ}$) of the tubes in the heat exchanger instead of inline ones ($\theta = 90^{\circ}$). By comparing the performance attributes of AR2 and AR3 with those of AR1 (all have the same area ratio ϕ = 2.4%), it is documented that increasing the radius ratio (λ) from 1/3 to 1/2 and 2/3, the *MMF* and the charging effectiveness are increased by 1.6%, 3.3%, and 3.9%, 8.1%, respectively. Also, the charging time is shortened by 7.2% when using AR3 instead of AR1.

In addition, the *MMF* and charging effectiveness are increased by 4.2% and 7.4%, respectively, as a result of incorporating SCTs (AR7) instead of CCTs (AR3) at the same radius ratio ($\lambda = 2/3$), the same area ratio (ϕ = 2.4%). Besides, the charging time is reduced by 7.3%. Furthermore, when comparing the performance attributes of AR4 with those of AR3 (both have the same radius ratio of $\lambda = 2/3$), it is noted that the *MMF* and charging effectiveness are increased by 20.4% and 19.7%, respectively, as the area ratio increases from 2.4% to 4.3%, and the corresponding charging time is reduced by 17.7%. Moreover, by distributing the same number of tubes in two layers (AR6) rather than one layer (AR4), the *MMF* and charging effectiveness are boosted by 3.7% and 8%, respectively, and the charging time is decreased by 11%. However, by applying staggered distribution of the tubes (AR6; $\theta = 45^{\circ}$) instead of an inline one (AR5; $\theta = 90^{\circ}$), the *MMF* and charging effectiveness are amplified by 1.8% and 5.3%, respectively, and the charging time is decreased by 2.9% at an HTFT of 75 °C.

These results can be attributed to increasing the radius ratio (λ) from 1/3 to 2/3, which provides a better distribution of the heat sources within the PCM as most of the PCM is in the outer area of the shell, which overcomes the poor thermal conductance of the PCM. Consequently, the charging process takes less time with more *MMF* and greater charging effectiveness. Furthermore, using SCTs instead of CCTs at λ and ϕ (AR3, AR7) increases the heat transfer surface area between the HTF and the

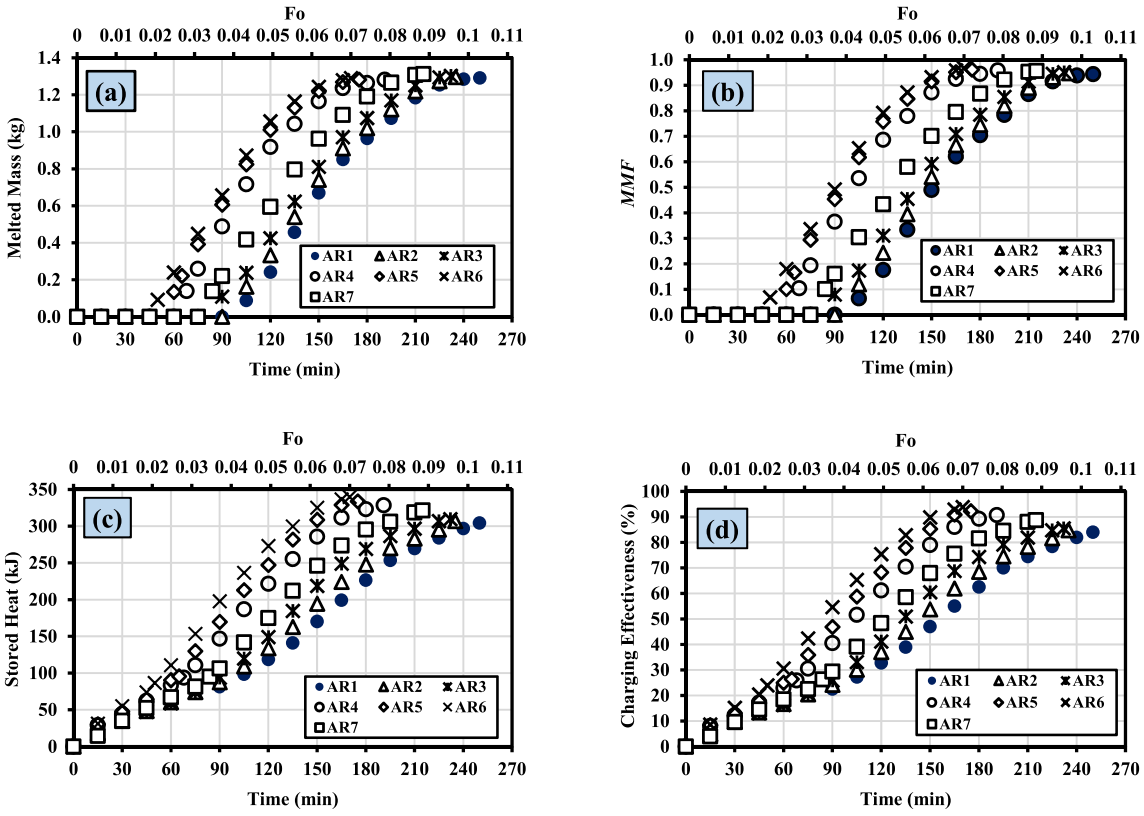

Fig. 10. Performance parameters versus charging time at different arrangements ($St \approx 0.233$); (a) Melted mass, (b) *MMF*, (c) Stored heat, (d) Charging effectiveness.

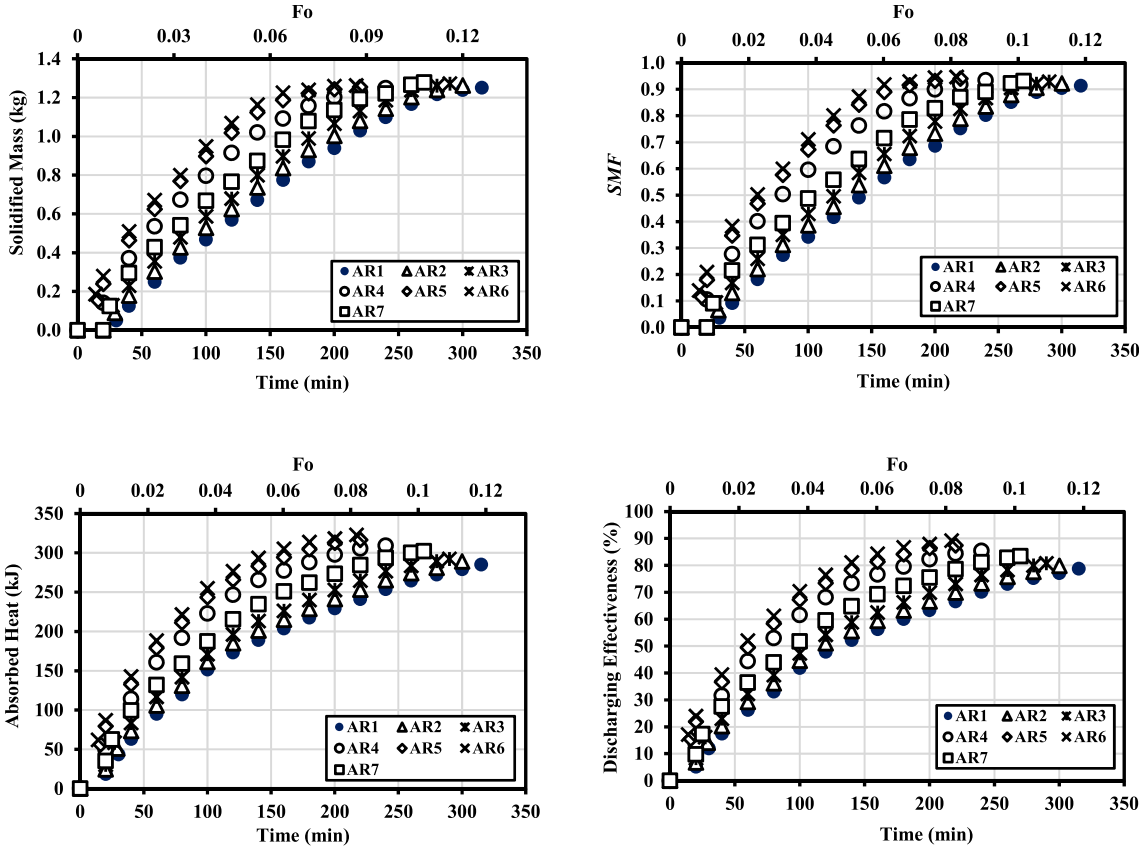

Fig. 11. Performance parameters versus discharging time at different arrangements ($St \approx 0.452$); (a) Solidified mass, (b) *SMF*, (c) Absorbed heat, (d) Discharging effectiveness.

adjacent PCM, which leads to enhanced system thermal performance/effectiveness and reduces the melting time. Moreover, increasing the number of internal tubes (area ratio ϕ) in the same layer in the shell (AR3, AR4) provides more heat sources and more heat transfer area between the HTF and the adjacent PCM, by which the system's thermal performance and charging effectiveness are augmented, the heat transfer process becomes faster, and the charging process takes a lesser time. Additionally, by distributing the heat sources in a staggered manner ($\theta = 45°$) through two layers instead of one in the shell (AR4, AR5, AR6), it boosts the LHTES system's performance, provides less melting time, and increases the charging effectiveness. This is due to reducing the PCM conduction resistance by decreasing the heat transfer path length between the heat sources (internal tubes).

7.3. Effect of heat exchanger configuration on the discharging process

The discharging (solidification) process is performed on the seven arrangements of the tested heat exchanger at an HTFT of 25 °C ($St = 0.452$) with a flow rate of 15.28 l/min. Fig. 11 illustrates the obtained results from the discharging processes (charging is at 70 °C HTFT) for the solidified mass fraction (*SMF*), accumulated absorbed heat, and discharging effectiveness due to using various heat exchanger configurations. It is obvious that increasing the radius ratio from 1/3 to 2/3, using SCTs instead of CCTs, increasing the number of internal tubes (area ratio ϕ), and applying staggered distribution ($\theta = 45°$) of the tubes in the heat exchanger boosts the discharging effectiveness by 2.6%, 3.3%, 5.7%, and 2.1%, respectively. Also, they augment the system's thermal performance and provide a shorter solidification time. These improvements in the results are due to the finest heat source distribution within the shell, which reduces the PCM conduction resistance besides the increase in the heat transfer area between the HTF tube and the adjacent PCM.

8. Correlations of the charging process

Utilizing the existing data in this work, correlations are introduced to predict the effectiveness of the present system for different arrangements through the charging process. As mentioned in Table 1, AR1, AR2, and AR3 have CCTs with the same number of tubes, area ratio (ϕ), and distribution angle (θ). Therefore, their charging effectiveness is correlated as a function of *Fo*, *St*, and the radius ratio (λ) as followed in Eqs. (19) and (20).

$$\varepsilon_{ch} = 651.602 Fo^{0.883} St^{0.244} \lambda^{0.038} \begin{bmatrix} 0.0062 \le Fo \le 0.0371 \\ 0.096 \le St \le 0.233 \\ 1/3 \le \lambda \le 2/3 \\ \theta = 90^{\circ} \\ N = 1 \\ \phi = 2.4\% \end{bmatrix} \quad (19)$$

$$\varepsilon_{ch} = 4830.655 Fo^{1.465} St^{0.209} \lambda^{0.27} \begin{bmatrix} 0.0371 \le Fo \le 0.1071 \\ 0.096 \le St \le 0.233 \\ 1/3 \le \lambda \le 2/3 \\ \theta = 90^{\circ} \\ N = 1 \\ \phi = 2.4\% \end{bmatrix} \quad (20)$$

Furthermore, AR4, AR5, and AR6 have CCTs of a fixed value of the area ratio ($\phi = 4.3\%$). Consequently, their charging effectiveness is correlated as a function of *Fo*, *St*, the number of layers (N), and the distribution angle (θ) as followed in Eqs. (21) and (22).

$$\varepsilon_{ch} = 769.431 Fo^{0.867} St^{0.362} N^{0.234} \left(\frac{\theta}{180}\right)^{-0.182} \begin{bmatrix} 0.0062 \le Fo \le 0.0247 \\ 0.096 \le St \le 0.233 \\ 45^{\circ} \le \theta \le 90^{\circ} \\ N = 1 or 2 \\ \phi = 4.3\% \end{bmatrix} \quad (21)$$

$$\varepsilon_{ch} = 3217.32 Fo^{1.313} St^{0.222} N^{0.313} \left(\frac{\theta}{180}\right)^{-0.176} \begin{bmatrix} 0.0247 \le Fo \le 0.0811 \\ 0.096 \le St \le 0.233 \\ 45^{\circ} \le \theta \le 90^{\circ} \\ N = 1 or 2 \\ \phi = 4.3\% \end{bmatrix} \quad (22)$$

Additionally, the charging effectiveness of AR7 (having SCTs) is correlated as a function of *Fo* and *St*, as in Eqs. (23) and (24).

$$\varepsilon_{ch} = 1095.568 Fo^{1.05} St^{0.129} \begin{bmatrix} 0.0062 \le Fo \le 0.0371 \\ 0.096 \le St \le 0.233 \\ \lambda = 2/3 \\ \theta = 90^{\circ} \\ N = 1 \\ \phi = 2.4\% \end{bmatrix} \quad (23)$$

$$\varepsilon_{ch} = 4286.708 Fo^{1.416} St^{0.192} \begin{bmatrix} 0.0371 \le Fo \le 0.0865 \\ 0.096 \le St \le 0.233 \\ \lambda = 2/3 \\ \theta = 90^{\circ} \\ N = 1 \\ \phi = 2.4\% \end{bmatrix} \quad (24)$$

The experimental outputs of ε_{ch} are compared with those predicted by the introduced correlations, as illustrated in Fig. 12, which presents a maximum deviation of ± 12.9%.

9. Conclusions

This work practically tests the performance attributes of an LHTES system in a vertical shell-tube heat exchanger configuration. The internal tubes are straight and arranged as circular layers at certain radii in the shell, which is occupied by PCM, while water flows in the tubes in an upward direction. The experiments consider the effects of the tube area ratio ($2.4\% \le \phi \le 4.3\%$), the layer radius ratio ($1/3 \le \lambda \le 2/3$), the number of tube layers ($N = 1$or2), and the distribution of the tubes in the shell: inline ($\theta = 90°$)/staggered ($\theta = 45°$). Besides, the effect of incorporating SCTs instead of CCTs is examined. These experiments are conducted at three different HTFTs (65, 70, and 75 °C) during the charging process, which corresponds to a wide range for the PCM Stefan Number ($0.096 \le St \le 0.233$), while an HTFT of 25 °C is considered during the discharging process. The runs are carried out for a Fourier Number up to 0.1071. As stated by the obtained outputs, increasing the HTF charging temperature (PCM Stefan Number) reduces the total charging time and raises both the *MMF* and charging effectiveness: increasing the HTFT from 65 to 75 °C leads to average variations of − 4.3% and + 5.4% in the melting time and charging effectiveness, respectively. Additionally, the heat exchanger configuration has a considerable influence on the system's thermal performance. These effects (at 75 °C and 25 °C charging/discharging temperatures) are as follows:

- By increasing the radius ratio (λ) from 1/3 to 2/3, the total experiment time is reduced by 7.2%, and the charging/discharging effectiveness is improved by 8.1% and 2.6%, respectively.
- Using SCTs instead of CCTs reduces the melting time by 7.3% and augments the charging/discharging effectiveness by 7.4% and 3.3%, respectively.
- Increasing the area ratio (ϕ) from 2.4% to 4.3% provides a reduction in the total charging time of 17.6% and improves the charging/discharging effectiveness by 19.7% and 5.7%, respectively.
- Distributing the same number of tubes in two layers rather than one layer delivers a reduction in the melting time of 11%, and the charging/discharging effectiveness is boosted by 8% and 4.5%, respectively.

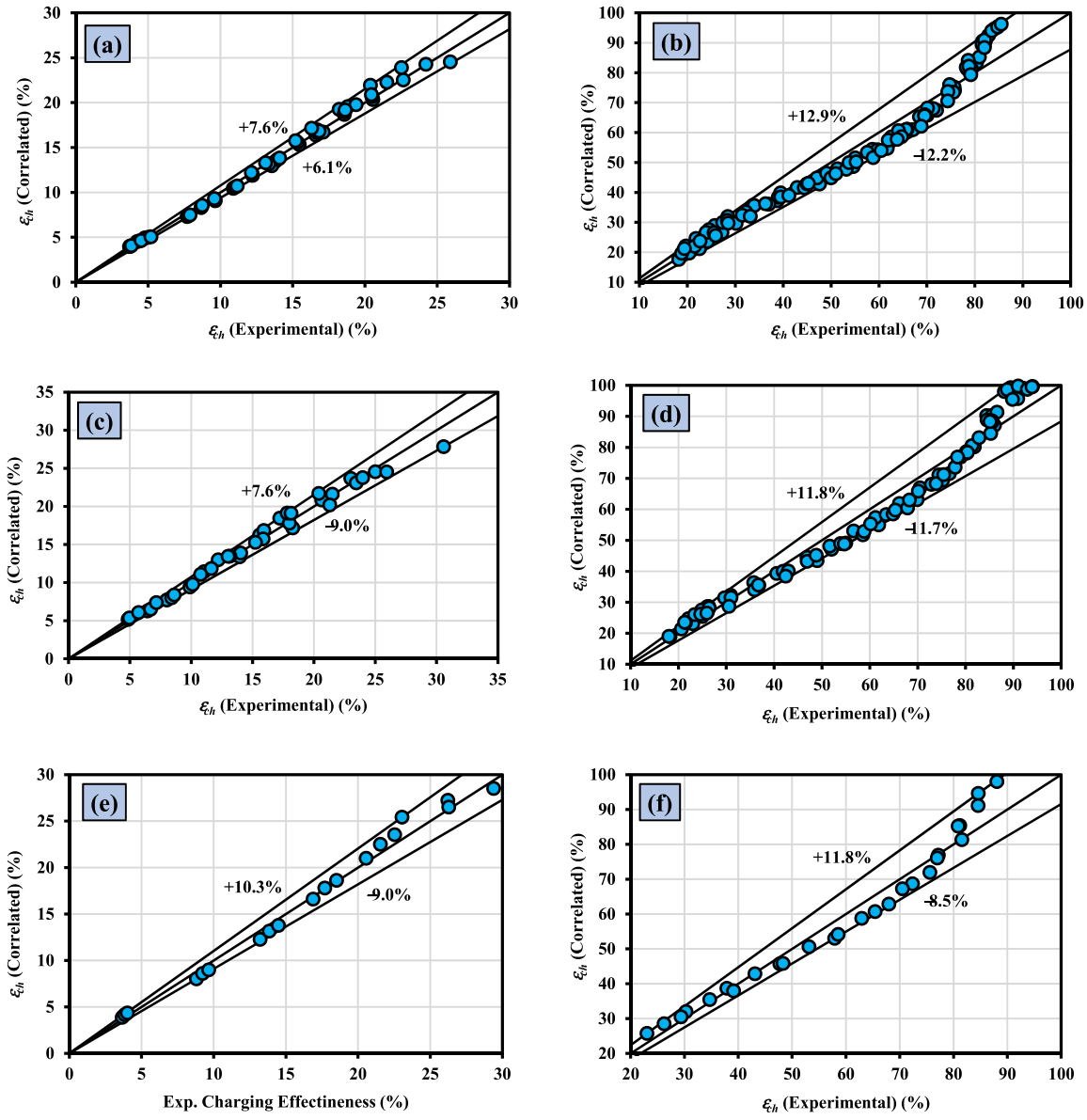

Fig. 12. Comparisons of the present experimental and correlated values of ε_{ch}; (a) Eq. (19), (b) Eq. (20), (c) Eq. (21), (d) Eq. (22), (e) Eq. (23) and (f) Eq. (24).

- Applying staggered distribution of the tubes instead of an inline one, the *MMF* and charging effectiveness are amplified by 1.8% and 5.3%, respectively.

Finally, a set of experimental correlations is developed to predict the charging effectiveness of the LHTES system.

Declaration of Competing Interest

The authors declare that they have no known competing financial interests or personal relationships that could have appeared to influence the work reported in this paper.

Data availability

Data will be made available on request.

Appendix A

To evaluate the uncertainty in the computed parameters, the effects of all variables are considered as recommended by Kline and McClintock [42];

$$\frac{\omega_{A_{t,o}}}{A_{t,o}} = \pm\sqrt{\left(\frac{2^{*}\omega_{D_{t,o}}}{D_{t,o}}\right)^{2}} = \pm\sqrt{\left(\frac{2^{*}0.1}{9.52}\right)^{2}} = \pm 0.021 = \pm 2.1\% \tag{A.1}$$

$$\frac{\omega_{A_{sh,in}}}{A_{sh,in}} = \pm\sqrt{\left(\frac{2*\omega_{D_{sh,in}}}{D_{sh,in}}\right)^2} = \pm\sqrt{\left(\frac{2*0.5}{120}\right)^2} = \pm 0.0083 = \pm 0.83\% \tag{A.2}$$

$$\frac{\omega_{V_{t,o}}}{V_{t,o}} = \pm\sqrt{\left(\frac{\omega_{A_{t,o}}}{A_{t,o}}\right)^2 + \left(\frac{\omega_L}{L}\right)^2} = \pm\sqrt{(0.021)^2 + \left(\frac{0.5}{135}\right)^2} = \pm 0.0213 = \pm 2.13\% \tag{A.3}$$

$$\frac{\omega_{V_{sh,in}}}{V_{sh,in}} = \pm\sqrt{\left(\frac{\omega_{A_{sh,in}}}{A_{sh,in}}\right)^2 + \left(\frac{\omega_L}{L}\right)^2} = \pm\sqrt{(0.0083)^2 + \left(\frac{0.5}{135}\right)^2} = \pm 0.0091 = \pm 0.91\% \tag{A.4}$$

$$\frac{\omega_V}{V} = \pm\frac{\sqrt{{\omega_{V_t}}^2 + {\omega_{V_{sh}}}^2}}{V} = \pm 0.00944 = \pm 0.94\% \tag{A.5}$$

$$\frac{\omega_{m_T}}{m_T} = \pm\sqrt{\left(\frac{\omega_{\rho_S}}{\rho_S}\right)^2 + \left(\frac{\omega_V}{V}\right)^2} = \pm\sqrt{(0.001)^2 + (0.0094)^2} = \pm 0.0095 = \pm 0.95\% \tag{A.6}$$

$$\omega_{\Delta T} = \pm\sqrt{(\omega_T)^2 + (\omega_T)^2} = \pm\sqrt{2*(0.5)^2} = \pm 0.71^{\circ}\mathrm{C} \tag{A.7}$$

$$\frac{\omega_{MMF}}{MMF} = \frac{\omega_{SMF}}{SMF} = \pm\sqrt{\left(\frac{\omega_m}{m}\right)^2 + \left(\frac{-\omega_{m_T}}{m_T}\right)^2} = \pm\sqrt{(0.0095)^2 + (0.0095)^2} = \pm 1.34\% \tag{A.8}$$

$$\frac{\omega_{Q_{sens.s}}}{Q_{sens,s}} = \pm\sqrt{\left(\frac{\omega_{m_T}}{m_T}\right)^2 + \left(\frac{\omega_{C_S}}{C_S}\right)^2 + \left(\frac{\omega_{\Delta T_s}}{\Delta T_s}\right)^2} = \pm 0.0235 = \pm 2.35\% \tag{A.9}$$

$$\frac{\omega_{Q_l}}{Q_l} = \pm\sqrt{\left(\frac{\omega_{m_T}}{m_T}\right)^2 + \left(\frac{\omega_{LH}}{LH}\right)^2} = \pm 0.0096 = \pm 0.96\% \tag{A.10}$$

$$\frac{\omega_{Q_{sens.L}}}{Q_{sens.L}} = \pm\sqrt{\left(\frac{\omega_{m_T}}{m_T}\right)^2 + \left(\frac{\omega_{C_L}}{C_L}\right)^2 + \left(\frac{\omega_{\Delta T_L}}{\Delta T_L}\right)^2} = \pm 0.0716 = \pm 7.16\% \tag{A.11}$$

$$\frac{\omega_Q}{Q} = \pm\frac{\sqrt{\omega_{Q_{sens.s}}^2 + \omega_{Q_l}^2 + \omega_{Q_{sens.L}}^2}}{Q} = \pm 0.0111 = \pm 1.11\% \tag{A.12}$$

$$\frac{\omega_\varepsilon}{\varepsilon} = \pm\sqrt{\left(\frac{\omega_Q}{Q}\right)^2 + \left(\frac{-\omega_Q}{Q_{max}}\right)^2} = \pm\sqrt{2\times(0.0111)^2} = \pm 0.0157 = \pm 1.57\% \tag{A.13}$$

References

[1] K. Pielichowska, K. Pielichowski, Phase change materials for thermal energy storage, Prog. Mater. Sci 65 (2014) 67–123.
[2] I. Dincer, M.A. Rosen, Thermal energy storage: systems and applications, 2nd edition, John Wiley & Sons, Ltd, 2010.
[3] M.R. Salem, M.M. Elsayed, A.A. Abd-Elaziz, K.M. Elshazly, Performance enhancement of the photovoltaic cells using Al_2O_3/PCM mixture and/or water cooling-techniques, Renew. Energy 138 (2019) 876–890.
[4] Q. He, S. Wang, M. Tong, Y. Liu, Experimental study on thermophysical properties of nanofluids as phase-change material (PCM) in low temperature cool storage, Energy Convers. Manag. 64 (2012) 199–205.
[5] T. Li, J. Lee, R. Wang, Y. Kang, Enhancement of heat transfer for thermal energy storage application using stearic acid nanocomposite with multi-walled carbon nanotubes, Energy 55 (2013) 752–761.
[6] T. Teng, C. Cheng, C. Cheng, Performance assessment of heat storage by phase change materials containing MWCNTs and graphite, Appl. Therm. Eng. 50 (2013) 637–644.
[7] T. Li, J. Lee, R. Wang, Y. Kang, Heat transfer characteristics of phase change nanocomposite materials for thermal energy storage application, Int. J. Heat Mass Transf. 75 (2014) 1–11.
[8] H. Al-Kayiem, S. Lin, Performance evaluation of a solar water heater integrated with a PCM nanocomposite TES at various inclinations, Sol. Energy 109 (2014) 82–92.
[9] A. Mosaffa, F. Talati, H. Tabrizi, M. Rosen, Analytical modeling of PCM solidification in a shell and tube finned thermal storage for air conditioning systems, Energy Build. 49 (2012) 356–361.
[10] A. Korti, F. Tlemsani, Experimental investigation of latent heat storage in a coil in PCM storage unit, J. Energy Storage 5 (2016) 17–186.
[11] N. Tay, M. Belusko, F. Bruno, Designing a PCM storage system using the effectiveness-number of transfer unit method in low energy cooling of buildings, Energy Build. 50 (2012) 234–242.
[12] M. Hosseini, A. Ranjbar, K. Sedighi, M. Rahimi, A combined experimental and computational study on the melting behavior of a medium temperature phase change storage material inside shell and tube heat exchanger, Int. Commun. Heat Mass Transf. 39 (9) (2012) 1416–1424.
[13] E. Guelpa, A. Sciacovelli, V. Verda, Entropy generation analysis for the design improvement of a latent heat storage system, Energy 53 (2013) 128–138.
[14] M. Avci, M. Yazici, Experimental study of thermal energy storage characteristics of a paraffin in a horizontal tube-in-shell storage unit, Energy Convers. Manag. 73 (2013) 271–277.
[15] M. Mahfuz, M. Anisur, M. Kibria, R. Saidur, I. Metselaar, Performance investigation of thermal energy storage system with phase change material (PCM) for solar water heating application, Int. Commun. Heat Mass Transf. 57 (2014) 132–139.
[16] B. Kamkari, H. Shokouhmand, F. Bruno, Experimental investigation of the effect of inclination angle on convection-driven melting of phase change material in a rectangular enclosure, Int. J. Heat Mass Transf. 72 (2014) 186–200.
[17] M. Hosseini, M. Rahimi, R. Bahrampoury, Experimental and computational evolution of a shell and tube heat exchanger as a PCM thermal storage system, Int. Commun. Heat Mass Transf. 50 (2014) 128–136.
[18] X. Sun, Q. Zhang, M. Medina, K. Lee, Experimental observations on the heat transfer enhancement caused by natural convection during melting of solid–liquid phase change materials (PCMs), Appl. Energy 162 (2016) 1453–1461.
[19] C. Abujas, A. Jove, C. Prieto, M. Gallas, L. Cabeza, Performance comparison of a group of thermal conductivity enhancement methodology in phase change material for thermal storage application, Renew. Energy 97 (2016) 434–443.
[20] S. Seddegh, X. Wang, A. Henderson, A comparative study of thermal behaviour of a horizontal and vertical shell-and-tube energy storage using phase change materials, Appl. Therm. Eng. 93 (2016) 348–358.
[21] G. Han, H. Ding, Y. Huang, L. Tong, Y. Ding, A comparative study on the performances of different shell-and-tube type latent heat thermal energy storage

units including the effects of natural convection, Int. Commun. Heat Mass Transf. 88 (2017) 228–235.
[22] M.S. Tayssir, S.M. Eldemerdash, R.Y. Sakr, A.R. Elshamy, O.E. Abdellatif, Experimental investigation of melting behavior of PCM by using coil heat source inside cylindrical container, J. Electr. Syst. Inf. Technol. 4 (1) (2017) 18–33.
[23] M. Mahdi, A. Hasan, H. Mahood, A. Campbell, A. Khadom, A. Karim, A. Sharif, Numerical study and experimental validation of the effects of orientation and configuration on melting in a latent heat thermal storage unit, J. Energy Storage 23 (2019) 456–468.
[24] S. Deng, C. Nie, G. Wei, W. Ye, Improving the melting performance of a horizontal shell-tube latent-heat thermal energy storage unit using local enhanced finned tube, Energy Build. 183 (2019) 161–173.
[25] D. Mehta, K. Solanki, M. Rathod, J. Banerjee, Thermal performance of shell and tube latent heat storage unit: comparative assessment of horizontal and vertical orientation, J. Energy Storage 23 (2019) 344–362.
[26] F. Fornarelli, S. Camporeale, B. Fortunato, Simplified theoretical model to predict the melting time of a shell-and-tube LHTES, Appl. Therm. Eng. 153 (2019) 51–57.
[27] J. Mahdi, S. Lohrasbi, D. Ganji, E. Nsofor, Simultaneous energy storage and recovery in the triplex-tube heat exchanger with PCM, copper fins and Al_2O_3 nanoparticles, Energy Convers. Manag. 180 (2019) 949–961.
[28] S. Pakalka, K. Valančius, G. Streckienė, Experimental comparison of the operation of PCM-based copper heat exchangers with different configurations, Appl. Therm. Eng. 172 (2020) 115138.
[29] S. Zhang, L. Pu, L. Xu, R. Liu, Y. Li, Melting performance analysis of phase change materials in different finned thermal energy storage, Appl. Therm. Eng. 176 (2020) 115425.
[30] H. Bazai, M.A. Moghimi, H.I. Mohammed, R. Babaei-Mahani, P. Talebizadehsardari, Numerical study of circular-elliptical double-pipe thermal energy storage systems, J. Energy Storage 30 (2020) 101440.
[31] O.S. Elsanusi, E.C. Nsofor, Melting of multiple PCMs with different arrangements inside a heat exchanger for energy storage, Appl. Therm. Eng. 185 (2021) 116046.
[32] F. He, J. Zou, X. Meng, W. Gao, L. Ai, Effect of copper foam fin (CFF) shapes on thermal performance improvement of the latent heat storage units, J. Energy Storage 45 (2022) 103520.
[33] H. Peng, W. Yan, Y. Wang, S. Feng, Discharging process and thermal evaluation in the thermal energy storage system with fractal tree-like fins, Int. J. Heat Mass Transf. 183(Part A) (2022) 122073.
[34] F.A. Rodrigues, M.J.S. de Lemos, Discharge effectiveness of thermal energy storage systems, App. Therm. Eng. 209 (2022) 118232.
[35] Z. Li, S.B. Oskouei, G. Fu, Ö. Bayer, L. Fan, Enhanced power density during energy charging of a shell-and-tube thermal storage unit: Comparison between the inclusion of metal fins and foams, J. Energy Storage 55 (Part C) (2022) 105576.
[36] Y. Shen, P. Zhang, A. Mazhar, H. Chen, S. Liu, Experimental analysis of a fin-enhanced three-tube-shell cascaded latent heat storage system, App. Therm. Eng. 213 (2022) 118717.
[37] M. Huang, W. He, A. Incecik, M.K. Gupta, G. Królczyk, Z. Li, Phase change material heat storage performance in the solar thermal storage structure employing experimental evaluation, J. Energy Storage 46 (2022) 103638.
[38] H.M. Ali, Phase change materials based thermal energy storage for solar energy systems, J. Build. Eng. 56 (2022) 104731.
[39] Q. Mao, Y. Zhang, Study on the thermal storage performance of a new cascade structure phase change thermal storage tank, J. Energy Storage 56 (Part C) (2022) 106155.
[40] J. Zou, F. He, Y. Qi, X. Meng, W. Ma, Thermal performance improvement of thermal energy storage systems by employing a contrastive experiment, Case Stud. Therm. Eng. 41 (2023) 102647.
[41] L. Lv, Y. Zou, S. Huang, X. Wang, R. Shao, X. Xue, Y. Rong, H. Zhou, Experimental study on a pilot-scale medium-temperature latent heat storage system with various fins, Renew. Energy 205 (2023) 499–508.
[42] S.J. Kline, F.A. McClintock, Describing uncertainties in single-sample experiments, Mech. Eng. 75 (1) (1953) 3–8.